VERSITA

Acta Geophysica
vol. 57, no. 4, pp. 981-1010
DOI: 10.2478/s11600-009-0027-4

Structure of Numerically Simulated Katabatic and Anabatic Flows along Steep Slopes

Evgeni FEDOROVICH and Alan SHAPIRO

School of Meteorology, University of Oklahoma, Norman, USA
e-mails: fedorovich@ou.edu (corresponding author), ashapiro@ou.edu

Abstract

Direct numerical simulation (DNS) is applied to investigate properties of katabatic and anabatic flows along thermally perturbed (in terms of surface buoyancy flux) sloping surfaces in the absence of rotation. Numerical experiments are conducted for homogeneous surface forcings over infinite planar slopes. The simulated flows are the turbulent analogs of the Prandtl (1942) one-dimensional laminar slope flow. The simulated flows achieve quasi-steady periodic regimes at large times, with turbulent fluctuations being modified by persistent low-frequency oscillatory motions with frequency equal to the product of the ambient buoyancy frequency and the sine of the slope angle. These oscillatory wave-type motions result from interactions between turbulence and ambient stable stratification despite the temporal constancy of the surface buoyant forcing. The structure of the mean-flow fields and turbulence statistics in simulated slope flows is analyzed. An integral dynamic similarity constraint for steady slope/wall flows forced by surface buoyancy flux is derived and quantitatively verified against the DNS data.

Key words: katabatic flow, anabatic flow, numerical simulation, boundary layer, turbulence.

1. INTRODUCTION

Slope winds (flows) are typical for vast areas of the Earth, and often play an important role in the weather and climate of these areas. From the standpoint of basic fluid dynamics, the slope winds are buoyantly driven boundary-

layer-type flows along heated or cooled sloping surfaces in a stratified fluid. Commonly, meteorologists distinguish between anabatic winds, which are driven by surface heating, and katabatic winds, which result from surface cooling. From the viewpoint of formal description and modeling, slope flows are challenging physical phenomena because they conflate three characteristic aspects of geophysical fluid dynamics: buoyant forcing, stratification, and turbulence. Although much progress has been made in the conceptual understanding and numerical simulation of the slope winds, there are still many open questions regarding the structure and properties of these flows. Of particular interest for practical applications are the mean-flow and turbulence structure of slope winds as functions of the surface thermal forcing and slope angle. Knowledge of these structural features of slope flows could be useful for designing parameterizations of slope-wind phenomena in atmospheric models.

In areas where basins are largely sheltered from synoptic effects, katabatic and anabatic flows are the building blocks of local weather. Even in cases where synoptic forcing is important, pronounced katabatic and anabatic flow signals may still be apparent. In regions where heavily industrialized population centers extend across variable topography (e.g., Los Angeles and Phoenix in the USA), these local flows exert major controls over energy usage, visibility, fog formation, and air pollutant dispersion (Lu and Turco 1994, Fernando *et al.* 2001, Hunt *et al.* 2003, Lee *et al.* 2003, and Brazel *et al.* 2005). In agricultural regions, these local winds significantly affect microclimates. They also need to be taken into account in aerial-spraying and fire-fighting operations. On the larger scale, persistent katabatic winds cover vast areas of the Earth (e.g., Greenland, Antarctica), and play an important role in the weather and climate of these areas (Parish and Waight 1987, Gallée and Schayes 1994, Oerlemans 1998, Renfrew 2004).

An early milestone in the conceptual understanding of katabatic/anabatic flows was the development of the Prandtl (1942) one-dimensional model for the laminar natural-convection flow of a viscous stably-stratified fluid along a uniformly cooled or heated sloping planar surface. Flow in the model has a boundary-layer character (low-level jet topped by weak reversed flow). The model solution, which is exact within the Boussinesq framework, satisfies conditions for both mechanical and thermodynamical equilibrium. The along-slope advection of environmental (mean) temperature balances thermal diffusion, and the along-slope component of buoyancy balances diffusion of along-slope momentum. All other terms in the equations of motion and thermodynamic energy are identically zero. Observations suggest that, with appropriately tuned mixing parameters, this simple model provides a good description of the vertical structure of slope flows at night and a reasonable approximation of slope flows during the day (e.g., Defant 1949, Ty-

son 1968, Papadopoulos *et al.* 1997, and Oerlemans 1998). With a suitable change of variables, the Prandtl model also describes the along-slope flow and perturbation salinity field in an oceanic mixing layer at a sloping sidewall (Phillips 1970, Wunsch 1970, and Peacock *et al.* 2004). In this oceanic context, the flow is generated solenoidally by isopycnals that are forced to approach the sloping boundary at a right angle (zero normal flux condition). The model also describes the free convective flow of a stratified fluid along heated vertical plates (Gill 1966, Elder 1965, and Shapiro and Fedorovich 2004a,b), and the familiar Ekman (1905) flow of a homogeneous viscous rotating fluid in the presence of an imposed wind stress or pressure gradient force (Batchelor 1967). The equivalence of the classical Prandtl and Ekman models is a remarkable manifestation of the general analogy between stratified and rotating flows (Veronis 1970).

Advances in computer technology have made possible numerical mesoscale modeling (Parish 1984, Parish and Waight 1987, Nappo and Rao 1987, Gallée and Schayes 1994, Atkinson 1981, Bromwich *et al.* 2001, Klein *et al.* 2001, Heinemann and Klein 2002, Rampanelli *et al.* 2004, Renfrew 2004) of slope winds and even numerical large eddy simulation (LES) of particular slope flow cases (see, e.g. Schumann 1990 and Skyllingstad 2003). Of particular interest for our research are results of those numerical studies that analyzed simulated slope flow dynamics in the context of conceptual models like the extended Prandtl model or the hydraulic model of Ball (1956). Nappo and Rao (1987), who applied an *e-l* turbulence closure to numerically study the spatial and temporal evolution of katabatic flows along finite-length slopes, found that ambient stratification profoundly affects the structure of the flow and, in the case of sufficiently long slope, ultimately results in a one-dimensional Prandtl-like flow regime. Heinemann and Klein (2002), Rampanelli *et al.* (2004), and Renfrew (2004) used three different state-of-the-art numerical model systems to reproduce idealized slope/valley winds with a remarkable degree of detail. The numerical results of Heinemann and Klein (2002) for Greenland katabatic winds show that flow patterns above vast portions of this island may be reasonably considered as two-dimensional, and allow interpretation in terms of Ball's theory. Rampanelli *et al.* (2004) looked at driving mechanisms of numerically reproduced upslope winds and found that basic features of observed flows in idealized two-dimensional settings are similar, as least qualitatively, to predictions of the Prandtl model. Renfrew's (2004) numerical study of Antarctic katabatic winds supported by analyses of field measurements also revealed a quasi-two-dimensional structure of the large-scale katabatic flow and pointed to the triggering of internal gravity waves which propagate energy away from the region of strongly decelerating flow. The theoretical analysis in Shapiro and Fedorovich (2007) also indicated that internal gravity waves would de-

velop in decelerating katabatic flows. All *op. cit.* numerical studies reported difficulties in finding an appropriate parameterization for the near-surface portion of the flow, which is either subject to strong buoyancy damping of turbulence in the case of katabatic flow or to absolute static instability inducing convective motions above a heated surface in the case of anabatic (upslope) wind.

The above-mentioned inherent shortcoming of the mesoscale modeling approach may be overcome, at least partially, within the LES framework. The LES has the potential to cover the gap between the mesoscale features of slope winds and the resolved, in an LES sense, turbulent motions that directly impact the dynamics of these flows. By resolving most of the energy-carrying motions, LES accounts for slope-flow turbulence effects in a much more accurate and consistent manner than do mesoscale models. However, this realism comes at a high computational cost. Nevertheless, reported LES studies of anabatic (Schumann 1990) and katabatic (Skyllingstad 2003) winds show that for small-scale (of the order of 1 to 10 km in the horizontal) slope flows, the LES method appears to be practicable.

In the study of Schumann (1990), LES was used to investigate the turbulent steady-state anabatic boundary layer along a uniformly heated, infinitely long inclined (in the limiting case – vertical) plate immersed in a stably stratified fluid. This setup permitted adoption of a quasi-homogeneity flow constraint in the along-plate direction, which made it much more tractable in the LES sense and permitted comparison with the classical Prandtl model. In fact, Schumann (1990) found that for small- and moderate-angle slope flows, fundamental predictions of the Prandtl theory are supported fairly well by the numerical results, apart from structural peculiarities of the flow. Among interesting findings of Schumann's (1990) study was the oscillatory behavior of momentum and temperature solutions, which was quite persistent and especially noticeable in the flow cases with large plate inclination angles. The frequency of these oscillations was $N \sin\alpha$ (N being the buoyancy frequency of the ambient fluid and α the plate inclination angle). Seeking to attain steady-state solutions for the simulated flow, Schumann (1990) forced damping of these oscillations by applying a specially designed solution relaxation algorithm. He did not, however, present an argument for a steady-state solution being the only possible terminal state of the flow.

Adapting an LES algorithm from oceanic studies to simulate spatially evolving atmospheric katabatic flow, Skyllingstad (2003) obtained insights into the structure of mean fields and turbulence characteristics in a three-dimensional flow setting without Coriolis effects or ambient stratification. In these simulations the slopes were relatively short and the flow was developing down slope from a state of rest. Accordingly, the quasi-homogeneous

flow (Prandtl-like) regime in the along-slope direction was not achieved in the simulations. The LES results suggested the importance of turbulence in controlling the strength and depth of katabatic flows, and revealed the shallowness of these flows when ambient winds were light. However, the subgrid closure used in Skyllingstad's (2003) study may not be optimal for the reproduction of stably stratified flow turbulence, so the reported results regarding the turbulent structure should be viewed with caution.

In the present study, the structural features of anabatic and katabatic flows are investigated using an updated version of the direct numerical simulation (DNS) code previously employed to study buoyantly driven flows along vertical plates and inclined surfaces with constant and time-dependent surface thermal perturbations (Shapiro and Fedorovich 2004b, 2005, 2006, 2008, Fedorovich and Shapiro 2009). The DNS experiments explore prototypical physical effects in idealized downscaled atmospheric slope flows with the goal of improving the conceptual understanding of the turbulence contribution to dynamics and thermodynamics of katabatic and anabatic winds. Particular emphasis is placed on studying the dependence of the mean profiles and turbulence statistics on the sign and magnitude of surface buoyancy forcing (in terms of surface buoyancy flux) and the slope steepness. Due to computational limitations and longer times needed to obtain steady statistics in the flows over shallow slopes (see Section 4), DNS runs are conducted only with slopes 30º and steeper.

The layout of the paper is as follows. The basic equations of slope flow dynamics in a doubly-infinite slope setting and corresponding boundary conditions are considered in Section 2. In Section 3, the Prandtl (1942) model solutions for slope flows are reviewed for the original slope-flow scenario with prescribed surface buoyancy, as well as for a flow resulting from a constant surface buoyancy flux (energy production rate). The numerical experiments and the subsequent simulation results are described in Section 4. Section 5 summarizes findings of the study.

2. EQUATIONS OF SLOPE FLOW DYNAMICS

Momentum balance equations for a small-scale (very large Rossby number) flow in the Boussinesq approximation are the following:

$$\frac{\partial u}{\partial t}+u\frac{\partial u}{\partial x}+v\frac{\partial u}{\partial y}+w\frac{\partial u}{\partial z}=-\frac{\partial \pi}{\partial x}+\beta\theta\sin\alpha+\nu\left(\frac{\partial^2 u}{\partial x^2}+\frac{\partial^2 u}{\partial y^2}+\frac{\partial^2 u}{\partial z^2}\right), \tag{1}$$

$$\frac{\partial v}{\partial t}+u\frac{\partial v}{\partial x}+v\frac{\partial v}{\partial y}+w\frac{\partial v}{\partial z}=-\frac{\partial \pi}{\partial y}+\nu\left(\frac{\partial^2 v}{\partial x^2}+\frac{\partial^2 v}{\partial y^2}+\frac{\partial^2 v}{\partial z^2}\right), \tag{2}$$

$$\frac{\partial w}{\partial t}+u\frac{\partial w}{\partial x}+v\frac{\partial w}{\partial y}+w\frac{\partial w}{\partial z}=-\frac{\partial \pi}{\partial z}+\beta\theta\cos\alpha+\nu\left(\frac{\partial^2 w}{\partial x^2}+\frac{\partial^2 w}{\partial y^2}+\frac{\partial^2 w}{\partial z^2}\right), \qquad (3)$$

with the heat balance given by

$$\frac{\partial \theta}{\partial t}+u\frac{\partial \theta}{\partial x}+v\frac{\partial \theta}{\partial y}+w\frac{\partial \theta}{\partial z}=-\gamma(u\sin\alpha+w\cos\alpha)+\nu_h\left(\frac{\partial^2 \theta}{\partial x^2}+\frac{\partial^2 \theta}{\partial y^2}+\frac{\partial^2 \theta}{\partial z^2}\right), \qquad (4)$$

and mass conservation represented by the continuity equation for an incompressible fluid,

$$\frac{\partial u}{\partial x}+\frac{\partial v}{\partial y}+\frac{\partial w}{\partial z}=0\,. \qquad (5)$$

In the above equations, u, v, w are velocity components in the right-hand slope-following Cartesian coordinate system (Fig. 1) with x, y and z being the upslope, cross-slope, and slope-normal coordinates, respectively, $\pi=[p-p_e(z')]/\rho_r$ is the normalized pressure perturbation ($p_e(z')$ is the environmental pressure, z' is the true vertical coordinate, $\rho_r=\text{const}$ is the reference density value), $\theta=\Theta-\Theta_e(z')$ is the potential temperature perturbation, $\gamma=\mathrm{d}\Theta_e/\mathrm{d}z'=\text{const}$ is the gradient of environmental potential temperature, $\beta=g/\Theta_r$ is the buoyancy parameter ($\Theta_r=\text{const}$ is the reference potential temperature value, g is the gravitational acceleration), α is the slope angle, ν is the kinematic viscosity, and ν_h is the thermal diffusivity.

The heat balance equation (4) may be rewritten in terms of the buoyancy $b=\beta\theta$ as

$$\frac{\partial b}{\partial t}+u\frac{\partial b}{\partial x}+v\frac{\partial b}{\partial y}+w\frac{\partial b}{\partial z}=-N^2(u\sin\alpha+w\cos\alpha)+\nu_h\left(\frac{\partial^2 b}{\partial x^2}+\frac{\partial^2 b}{\partial y^2}+\frac{\partial^2 b}{\partial z^2}\right), \qquad (6)$$

where $N=(\beta\gamma)^{1/2}$ is the Brunt–Väisälä (or buoyancy) frequency.

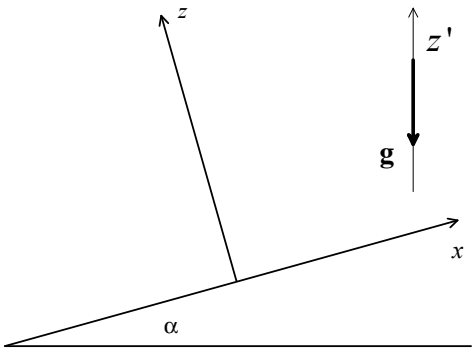

Fig. 1. Slope-following coordinate system.

The lateral boundary conditions for prognostic variables (u, v, w, b) and normalized pressure π are periodic (the sloping surface is supposed to be doubly-infinite along x and y). The upper boundary conditions (large z) are $\partial\varphi/\partial z = 0$, where φ is any of (u, v, w, b), and $\partial\pi/\partial z$ is obtained from (3). The surface ($z = 0$) conditions are no-slip and impermeability ($u = v = w = 0$), with $\partial\pi/\partial z$ obtained from (3), and $\nu_h(\partial b/\partial z) = -B_s$, where B_s is the surface buoyancy flux which also has a meaning of the surface energy production rate.

3. PRANDTL MODEL OF SLOPE FLOW

Consider the following reduced version of (1)-(3) and (6) for the case of a stationary laminar flow parallel to the slope, which corresponds to the slope flow model of Prandtl (1942), though with $\nu = \nu_h$:

$$b\sin\alpha + \nu\frac{\partial^2 u}{\partial z^2} = 0\,, \tag{7}$$

$$-N^2 u\sin\alpha + \nu\frac{\partial^2 b}{\partial z^2} = 0\,, \tag{8}$$

with the following boundary conditions: $u(0) = 0$, $b(0) = b_s$ or $-\nu(\mathrm{d}b/\mathrm{d}z)\big|_{z=0} = B_s$, and $u \to 0$ and $b \to 0$ as $z \to 0$. The controlling parameters of the reduced problem are therefore α, ν, N, and either b_s or B_s.

Introducing generic length L, velocity V, and buoyancy B scales, and applying these scales in eqs. (7) and (8), we obtain the following non-dimensionalized momentum and buoyancy balance equations of the Prandtl model:

$$b_n + \frac{\nu V}{L^2\sin\alpha B}\,\frac{\partial^2 u_n}{\partial z_n^{\,2}} = 0\,, \tag{9}$$

$$-u_n + \frac{\nu B}{L^2\sin\alpha N^2 V}\,\frac{\partial^2 b_n}{\partial z_n^{\,2}} = 0\,, \tag{10}$$

with the boundary conditions transforming into $u_n(0) = 0$, and $u_n \to 0$, $b_n \to 0$ as $z_n \to \infty$, and either $b_n(0) = b_s/B$ (hereafter called the type I surface condition; the condition actually considered by Prandtl) or $(\mathrm{d}b_n/\mathrm{d}z_n)\big|_{z_n=0} = -B_s/\nu\cdot L/B$ (hereafter called the type II surface condition).

3.1 Type I surface condition

Assigning length, velocity, and buoyancy scales as $L = \nu^{1/2}N^{-1/2}\sin^{-1/2}\alpha$, $V = b_s N^{-1}$, and $B = b_s$, eqs. (9) and (10) may be reduced to

$$b_n + \frac{\partial^2 u_n}{\partial z_n^{\,2}} = 0\,, \quad -u_n + \frac{\partial^2 b_n}{\partial z_n^{\,2}} = 0\,, \tag{11}$$

where $z_n = z\nu^{-1/2}N^{1/2}\sin^{1/2}\alpha$, $u_n = ub_s^{-1}N$, and $b_n = bb_s^{-1}$, with the boundary conditions: $u_n(0) = 0$, $b_n(0) = 1$, and $u_n \to 0$, $b_n \to 0$ as $z_n \to \infty$. This problem has the following analytical solution (Shapiro and Fedorovich 2004a):

$$u_n = \sin(z_n/\sqrt{2})\exp(-z_n/\sqrt{2})\,, \quad b_n = \cos(z_n/\sqrt{2})\exp(-z_n/\sqrt{2})\,, \tag{12}$$

whose dimensional forms are identical to the original Prandtl model solutions. As demonstrated in Shapiro and Fedorovich (2004a), the peak normalized velocity, $u_{n\max} = (1/\sqrt{2})\exp(-\pi/4)$, occurs in this flow case at $z_{n\max} = \pi\sqrt{2}/4$.

Assuming values of the external parameters characteristic of atmospheric slope winds: $\nu = 1$ m^{2}s^{-1}, $N = 10^{-2}$s^{-1}, and $b_s = 10^{-1}$m s^{-2}, we come up with $u_{\max} = 3.2$ m s^{-1} at $z_{\max} = 12$ m for $\alpha = 60°$, at $z_{\max} = 16$ m for $\alpha = 30°$, and at $z_{\max} = 83$ m for $\alpha = 1°$.

Thus, with the prescribed constant surface buoyancy (surface condition of type I), the velocity maximum in the Prandtl model is independent of the slope angle, but the elevation of this maximum increases with decreasing slope angle as $\sin^{-1/2}\alpha$.

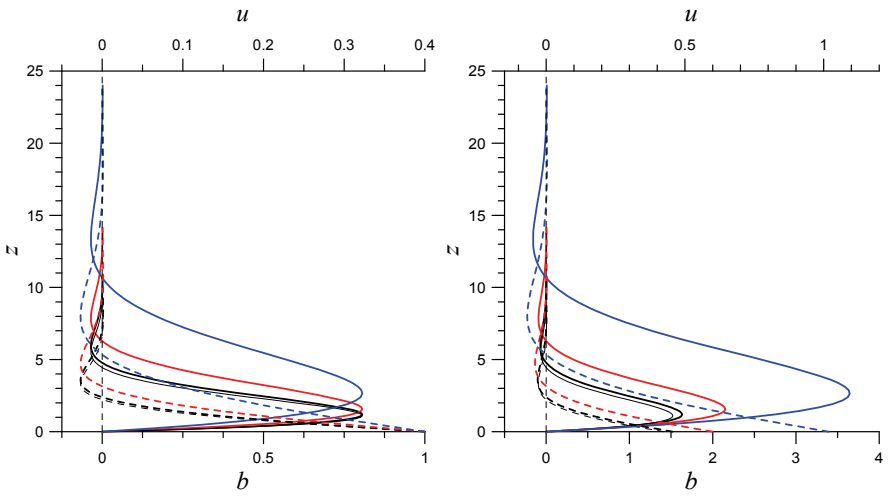

Fig. 2. Velocity u (in m s^{-1}, solid lines) and buoyancy b (in m s^{-2}, dashed lines) profiles (z is in meters) from the Prandtl model with type I ($b_s = 10^{-1}$ m s^{-2}, left) and type II ($B_s = 1$ m^{2}s^{-3}, right) surface conditions for different values of slope angle α: 90° (thin black lines), 60° (black lines), 30° (red lines), and 10° (blue lines) for $\nu = 1$ m^{2}s^{-1}, $N = 10^{-2}$s^{-1}.

Dimensional u [m s^{-1}] and b [m s^{-2}] profiles, calculated from (12) with $\nu = 1$ m^{2}s^{-1}, $N = 1$ s^{-1}, $b_s = $ m s^{-2}, are shown in Fig. 2 (left plot). They illustrate the dependence of the Prandtl model solution on the slope angle for the case of slope flow with constant surface buoyancy.

3.2 Type II surface condition

Redefining the length, velocity, and buoyancy scales as $L = \nu^{1/2} N^{-1/2} \sin^{-1/2}\alpha$, $V = \nu^{-1/2} N^{-3/2} B_s \sin^{-1/2}\alpha$, $B = \nu^{-1/2} N^{-1/2} B_s \sin^{-1/2}\alpha$, respectively, reduces the dimensionless problem (9)-(10) with the surface condition of type II to

$$b_n + \frac{\partial^2 u_n}{\partial z_n^{\,2}} = 0\,, \quad -u_n + \frac{\partial^2 b_n}{\partial z_n^{\,2}} = 0\,, \tag{13}$$

where $z_n = z\nu^{-1/2} N^{1/2} \sin^{1/2}\alpha$, $u_n = u\nu^{1/2} N^{3/2} B_s^{-1} \sin^{1/2}\alpha$, $b_n = b\nu^{1/2} N^{3/2} B_s^{-1} \sin^{1/2}\alpha$, with the boundary conditions $u_n(0) = 0$, $(\mathrm{d}b_n / \mathrm{d}z_n)\big|_{z_n = 0} = -1$, and $u_n \to 0$, $b_n \to 0$ as $z_n \to \infty$. This problem has the following analytical solution (Shapiro and Fedorovich 2004a):

$$u_n = \sqrt{2}\sin(z_n/\sqrt{2})\exp(-z_n/\sqrt{2})\,, \quad b_n = \sqrt{2}\cos(z_n/\sqrt{2})\exp(-z_n/\sqrt{2})\,. \tag{14}$$

In this case, as in the case of type I surface boundary condition, the peak normalized velocity also occurs at $z_{n\max} = \pi\sqrt{2}/4$, but now it has a different magnitude of $u_{n\max} = \exp(-\pi/4)$. Assuming typical atmospheric values of external parameters: $\nu = 1$ m^{2}s^{-1}, $N = 10^{-2}$ s^{-1}, and $B_s = 10^{-2}$ m^{2}s^{-3}, we find $u_{\max} = 4.9$ m s^{-1} at $z_{\max} = 12$ m for $\alpha = 60°$, $u_{\max} = 6.5$ m s^{-1} at $z_{\max} = 16$ m for $\alpha = 30°$, and $u_{\max} = 35$ m s^{-1} at $z_{\max} = 83$ m for $\alpha = 1°$. Thus, with the prescribed constant surface buoyancy flux, both the velocity maximum and the elevation at which the maximum occurs increase with decreasing slope angle as $\sin^{-1/2}\alpha$.

Dimensional u [m s^{-1}] and b [m s^{-2}] profiles in Fig. 2 (right plot), calculated from (14) with $\nu = 1$ m^{2}s^{-1}, $N = 1$ s^{-1}, and $B_s = 1$ m^{2}s^{-3}, illustrate the dependence of the Prandtl model solution on the slope angle for the case of slope flow driven by a constant surface buoyancy flux.

4. NUMERICAL SIMULATION OF TURBULENT SLOPE FLOWS

In the present study, idealized turbulent anabatic and katabatic flows along double-infinite slopes are investigated using direct numerical simulation (DNS), which implies resolving all scales of turbulent motion down to the viscous dissipation scale. The numerical algorithm employed to directly solve (1)-(3), (5) and (6) with $\mathrm{Pr} = \nu/\nu_h = 1$ is generally the same as the one

used to reproduce laminar (Shapiro and Fedorovich 2004b, 2006) and turbulent (Fedorovich and Shapiro 2009) convection flows of a stably stratified fluid along a heated vertical plate, which may be considered a case of an ultimately steep heated sloping surface, and turbulent katabatic flows along a homogeneously cooled sloping surface (Shapiro and Fedorovich 2008).

In the current version of the numerical code, the time advancement is performed with a hybrid leapfrog/Adams-Moulton third-order scheme (Shchepetkin and McWilliams 1998). The spatial derivatives are approximated by second-order finite-difference expressions on a staggered grid. The Poisson equation for pressure is solved with a fast Fourier transform technique over the *x*-*y* planes and a tri-diagonal matrix inversion method in the slope-normal direction. No-slip and impermeability conditions are applied on the velocity field at the slope surface. Equation (3) is used to formulate a Neumann boundary condition for the pressure at the surface and at the outer boundary of the domain (large *z*). Normal gradients of prognostic variables (velocity components and buoyancy) are set to zero at the outer computational boundary, and periodic boundary conditions are imposed at the *x*-*z* and *y*-*z* boundaries of the computational domain.

4.1 Parameters of simulated flows

We investigate idealized turbulent anabatic and katabatic flows along double-infinite slopes using DNS. The values of the surface buoyancy flux B_s are taken as –0.3 m^2s^{-3}, –0.5 m^2s^{-3} for the katabatic flow cases and 0.3 m^2s^{-3}, 0.5 m^2s^{-3} for the anabatic flow cases. Each flow type is investigated with the slope angle α of 30º and 60º. For comparison, data from the Fedorovich and Shapiro (2009) study of turbulent flow along a vertical heated wall ($\alpha = 90°$) are also considered.

In the wall-flow case ($\alpha = 90°$), the magnitudes of all flow variables are unchanged when the sign of the surface buoyancy flux B_s changes from positive (heated wall) to negative (cooled wall). Although the signs of the mean velocity, buoyancy, and turbulent fluxes of momentum and heat reverse, the variances of the velocity components and buoyancy remain invariant with respect to the sign of the surface buoyancy forcing.

Consideration of the averaged slope flow provides a convenient framework for the analysis of the DNS data. Applying the Reynolds decomposition to the flow variables in the governing equations (1)-(3) and (6) and averaging these equations over time and spatially over *x*-*y* planes parallel to the slope, we obtain:

$$\overline{b}\sin\alpha + \nu\frac{\partial^2\overline{u}}{\partial z^2} - \frac{\partial\overline{u'w'}}{\partial z} = 0\,, \tag{15}$$

$$-N^2\overline{u}\sin\alpha+\nu\frac{\partial^2\overline{b}}{\partial z^2}-\frac{\partial\overline{b'w'}}{\partial z}=0\,, \tag{16}$$

$$-\frac{\partial\overline{\pi}}{\partial z}+\overline{b}\cos\alpha-\frac{\partial\overline{w'w'}}{\partial z}=0\,, \tag{17}$$

where primes signify deviations from averages, denoted by overbars. Equation (17) integrates to $\overline{\pi}=-\overline{w'w'}-\cos\alpha\int_z^\infty \overline{b}\,\mathrm{d}z$ given that both $\overline{\pi}$ and $\overline{w'w'}$ vanish at $z=\infty$. Boundary conditions for eqs. (15) and (16) are: $\overline{u}=0$, $-\nu(\mathrm{d}\overline{b}/\mathrm{d}z)=B_s$ at $z=0$ (surface) and $\overline{u}=0$, $\overline{b}=0$ as $z\to\infty$ (far away from the slope). The turbulent fluxes are supposed to vanish on the surface and far above the slope.

Integrating (16) over z from 0 to ∞ and noting that both molecular and turbulent fluxes of the buoyancy vanish at ∞, we obtain an integral form of the buoyancy balance:

$$V_I L_I\equiv\int_0^\infty\overline{u}\,\mathrm{d}z=\frac{B_s}{N^2\sin\alpha}\,, \tag{18}$$

where the product $V_I L_I$ is the volume flux. Note that we do not define either the integral velocity scale V_I or the integral length scale $L_I\equiv\int_0^\infty(\overline{u}/V_I)\mathrm{d}z$.

As follows from eq. (18), katabatic and anabatic flows represented by the same value of $|B_s|/(N^2\sin\alpha)$ should have the same absolute value of the mean velocity integral. Therefore, the relation (18) may be interpreted as an **integral dynamic similarity constraint** for slope flows forced by the surface buoyancy flux (note that this criterion applies to both turbulent and laminar slope flows).

Based on the above considerations, one may introduce an integral slope-flow Reynolds number as

$$\mathrm{Re}_\mathrm{I}\equiv\frac{|V_I L_I|}{\nu}=\frac{|B_s|}{\nu N^2\sin\alpha}\equiv\frac{|\mathrm{Fp}_B|}{\sin\alpha}\,, \tag{19}$$

where the dimensionless combination

$$\mathrm{Fp}_B\equiv B_s\,\nu^{-1}N^{-2}\,, \tag{20}$$

hereafter called the **flow forcing parameter**, is negative for a katabatic flow ($B_s<0$) and positive for an anabatic flow ($B_s>0$). The magnitude of Fp_B represents the ratio between the energy production at the surface and the

work against buoyancy and viscous forces. From this definition of Re_I, we expect a particular slope flow to be more turbulent with increasing $|\mathrm{Fp}_B|$.

In the performed DNS, values of Re_I were within the range of 3000 to 10,000. These values were large enough to obtain reasonably developed turbulence while allowing use of relatively compact numerical grids and providing sufficiently long time series of variables to track the flow development. The simulations were conducted on the $x\times y\times z = 256\times 256\times N_z$ uniformly-spaced ($\Delta x = \Delta y = \Delta z = \Delta$) grids, with N_z varying from 400 to 800 depending on the Re_I of the simulated flow. The grid spacing Δ was chosen to ensure that the resolvability condition $\Delta \le 2L_m$ is satisfied (Pope 2000), with $L_m = \nu^{3/4}|B_s|^{-1/4}$ being an analog of the Kolmogorov microscale.

Noting that the dimensional governing parameters of the slope flow ν, N, and B_s have, respectively, dimensions of [$\mathrm{L}^2\,\mathrm{T}^{-1}$], [$\mathrm{T}^{-1}$], and [$\mathrm{L}^2\,\mathrm{T}^{-3}$], one can introduce some generic slope flow scales L (for distance), V (for velocity), and B (for buoyancy), and, based on the Π theorem (Langhaar 1951), write

$$L = \nu^{1/2}N^{-1/2}f_L(\mathrm{Fp}_B), \quad V = \nu^{1/2}N^{1/2}f_V(\mathrm{Fp}_B), \quad B = \nu^{1/2}N^{3/2}f_B(\mathrm{Fp}_B), \quad (21)$$

where f_L, f_V, and f_B, are functions of the dimensionless forcing parameter $\mathrm{Fp}_B = B_s\nu^{-1}N^{-2}$. Normalizing the averaged momentum and buoyancy balance equations (15) and (16) with the scales given in (21) we obtain the following scaled equations:

$$b_n\sin\alpha + \frac{f_V}{f_L^{\,2}f_B}\frac{\partial^2 u_n}{\partial z_n^{\,2}} - \frac{f_V^{\,2}}{f_L f_B}\frac{\partial\left(\overline{u'w'}\right)_n}{\partial z_n} = 0, \quad (22)$$

$$-u_n\sin\alpha + \frac{f_B}{f_L^{\,2}f_V}\frac{\partial^2 b_n}{\partial z_n^{\,2}} - \frac{f_B}{f_L}\frac{\partial\left(\overline{b'w'}\right)_n}{\partial z_n} = 0, \quad (23)$$

with normalized boundary conditions:

$$u_n = 0 \quad \text{and} \quad \frac{\mathrm{d}b_n}{\mathrm{d}z_n} = -\mathrm{Fp}_B\frac{f_L}{f_B} \quad \text{at} \quad z_n = 0, \quad (24)$$

$$u_n \to 0 \quad \text{and} \quad b_n \to 0 \quad \text{as} \quad z_n \to \infty, \quad (25)$$

where $z_n = z/L$, $u_n = \overline{u}/V$, $b_n = \overline{b}/B$, $\left(\overline{u'w'}\right)_n = \overline{u'w'}/V^2$, and $\left(\overline{b'w'}\right)_n = \overline{b'w'}/(VB)$.

Equations (22)-(25) indicate that for a given slope angle α, any scaling relationship for L, V and B, which results in the same $\mathrm{Fp}_B = B_s\nu^{-1}N^{-2}$, should

yield u_n, b_n, $\left(\overline{u'w'}\right)_n$, and $\left(\overline{b'w'}\right)_n$ that are universal functions of z_n. A particular form of the discussed universal behavior for the special case of buoyantly driven flow along a heated vertical wall, where $\sin\alpha = 1$ and $\mathrm{Re}_I = \mathrm{Fp}_B > 0$, has been numerically verified in Fedorovich and Shapiro (2009).

4.2 Spatial and temporal evolution of simulated slope flows

The spatial (in the z direction) and temporal evolution of the simulated velocity (u component) and buoyancy b fields in the central point of the x-y plane is illustrated in Fig. 3. Results are shown for katabatic flows with the same value of $\mathrm{Fp}_B = B_s \nu^{-1} N^{-2} = -5000$, but with two different slope angles: 30° and 60°. After passing through relatively short transition stages, both flows become turbulent. They display random, large-amplitude fluctuations of velocity and buoyancy fields in the core regions, where their behavior is characteristic of a developed turbulent flow, and show a quasi-periodic oscillatory behavior at larger distances from the slope. Notably, only fluctuations with a frequency equal to the natural buoyancy frequency $N\sin\alpha$ in the environmental fluid dominate at large z. Fluctuations with other frequencies rapidly decay away from the slope beyond the turbulent core of the flow. These dominant $N\sin\alpha$ oscillations are apparent far beyond the thermal and dynamic turbulent boundary layers developing along the slope. Note that the red shading in the color bar was chosen to draw attention to the weak return flow (positive u) and positively buoyant air above the primary katabatic jet.

The thermal boundary layers, whose depth may be estimated from the position of a narrow white region separating areas of negative (blue) and positive (red) buoyancy values, in both flow cases are considerably shallower than the corresponding dynamic boundary layers, whose depth is marked by the transition region (white) between the down-slope flow (blue) and up-slope return flow (red). It can be noted, however, that have we defined the top of the dynamic boundary to be the height of the jet, the thermal and dynamic boundary layers will be of comparable thickness. The overall thicknesses of the primary katabatic jet as well as the magnitudes of the buoyancy and velocity in the katabatic jet are larger in the 30° slope case than in the 60° slope case (note that values of all other controlling parameters of the flows are the same). This indicates that the qualitative prediction of the Prandtl model regarding the intensification and vertical expansion of the slope flow with decreasing slope angle in the case of specified surface buoyancy flux (cf. with right plot of Fig. 2), which applies − strictly speaking − only to a laminar slope flow, holds also for a turbulent slope flow.

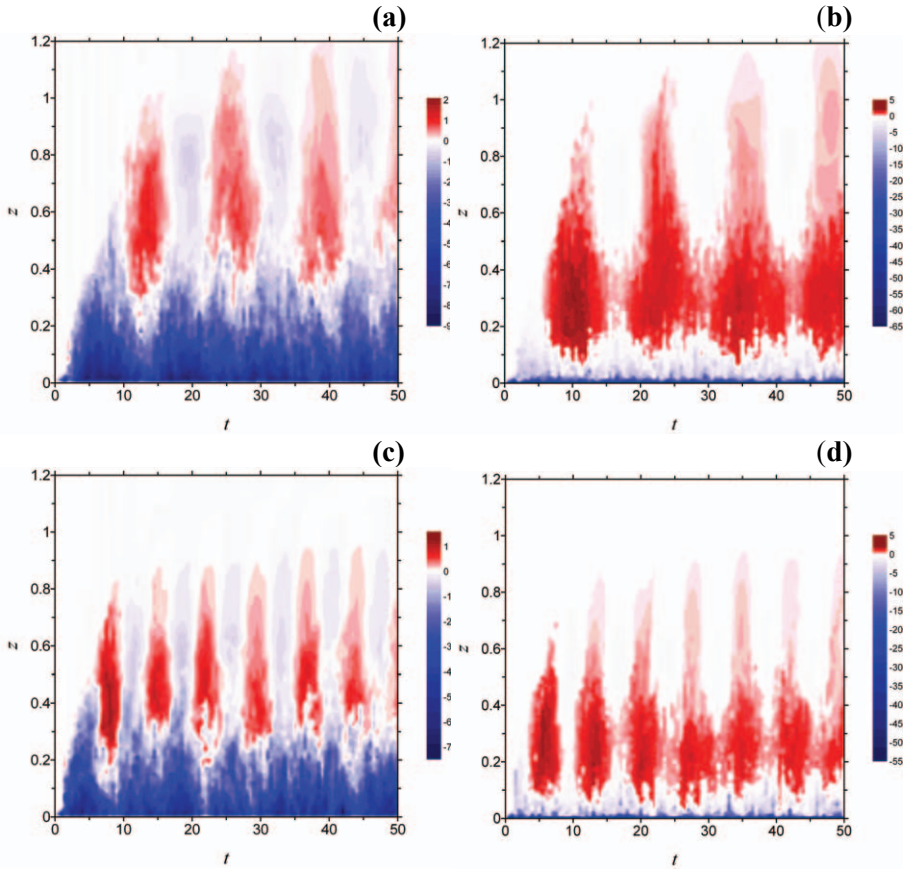

Fig. 3. Temporal variations of along-slope velocity component (u, plots a and c, in m s^{-1}) and buoyancy (b, plots b and d, in m s^{-2}) at different distances from the slope in the center of simulation domain for the katabatic flow cases ($B_s = -0.5$ m^{2}s^{-3}, $\nu = 10^{-4}$ m^{2}s^{-1}, $N = 1$ s^{-1}, resulting in $\mathrm{Fp}_B = -5000$) along slopes of different steepness: 30° (plots a and b) and 60° (plots c and d). Distance is in meters and time is in seconds.

An oscillatory flow pattern similar to the patterns shown in Fig. 3 was observed by Shapiro and Fedorovich (2006) in their study of a laminar natural convection flow along a wall with a temporally periodic surface thermal forcing. In the present case, however, the oscillatory flow motions result from interactions between turbulence and ambient stable stratification under the conditions of a temporally constant surface buoyancy forcing. Direct estimation of the oscillation period T from the plotted data provides T values very close to $2\pi/(N\sin\alpha)$ for each of the two considered slope angles: $T = 12.6$ s for $\alpha = 30°$ and $T = 7.3$ s for $\alpha = 60°$. Analogous flow oscillations

have been encountered by Schumann (1990) in large eddy simulations of anabatic winds (see discussion in the Introduction) and predicted/observed in the katabatic wind studies of Monti *et al.* (2002) and Princevac *et al.* (2008), where the frequency $N\sin\alpha$ has been identified as the frequency of the internal gravity waves that arrive normal to the slope.

The flow evolution patterns in Fig. 3 reveal that both simulated katabatic flows become statistically quasi-stationary with time. Such a quasi-stationarity of established katabatic flow is additionally illustrated in Fig. 4, where the u-velocity component and buoyancy fields averaged over x-y planes parallel to the slope are shown at increasing distances from the surface. The counterpart velocity and buoyancy distributions in an anabatic flow are demonstrated in Fig. 5. The presented time series of u and b refer to times in the simulation well beyond the transition stages, that is, after flows have evolved from the laminar to the developed turbulent state. A typical duration of the transition stage in the conducted simulations is about several seconds.

In the katabatic flow case (Fig. 4), the buoyancy field displays strong temporal variability in the turbulent core of the flow (at $z = 0.07$ m), where variability of the velocity field is also significant. Deeper into the flow, at $z = 0.3$ m, the magnitude of the buoyancy fluctuations drops noticeably while the average buoyancy changes its sign, which indicates that the considered elevation is in the relatively warm layer that caps the katabatic jet. However, the average velocity at $z = 0.3$ m remains negative, indicating that the flow at this level is still, on average, within the dynamic boundary layer. Such a vertical phase difference between the velocity and buoyancy profiles is another feature of the simulated turbulent flow that is qualitatively consistent with predictions of the Prandtl model (see right plot of Fig. 2). The discussed flow feature is clearly also seen in the spatial and temporal flow patterns presented in Fig. 4. The buoyancy field variations at $z = 0.3$ m are almost periodic with frequency $N\sin\alpha$, while the variability of the average velocity at this level still happens on a relatively broad range of time scales, but with the modulation of velocity fluctuations by the dominant mode oscillation already evident. At $z = 0.6$ m, the remaining random fine-scale fluctuations of both velocity and buoyancy become very small compared to the internal gravity wave oscillation, with the flow oscillation at $z = 0.9$ m being almost purely periodic and entirely determined by the internal gravity waves.

Time series of velocity and buoyancy in the anabatic flow (Fig. 5) show the variability features that are in many respects similar to the above discussed features of the katabatic flow. Far away from the slope, small-scale flow fluctuations associated with turbulent motions become negligible and the residual variability is entirely due to the internal-wave oscillations.

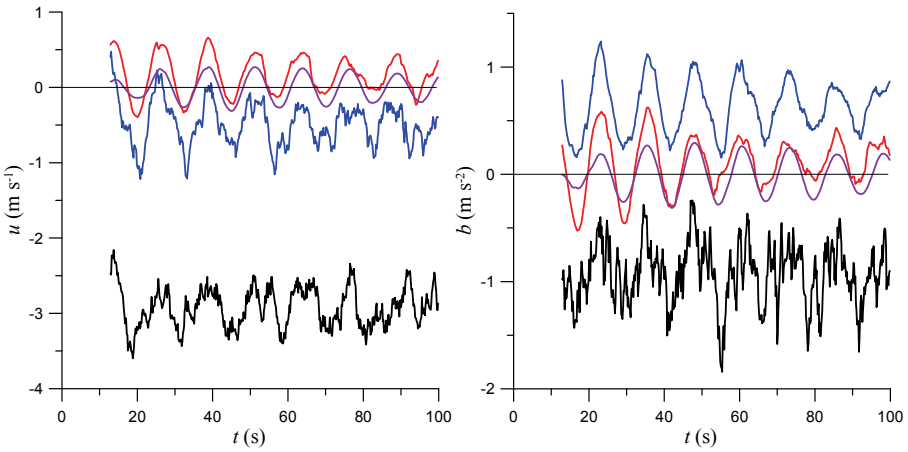

Fig. 4. Temporal evolution of the (x-y) plane-averaged velocity (left plot) and buoyancy (right plot) fields in the katabatic flow with $B_s = -0.3$ m^{2}s^{-3}, $\nu = 10^{-4}$ m^{2}s^{-1}, and $N = 1$ s^{-1} (Fp$_B = -3000$) along a 30°-slope at four different distances from the slope: 0.07 m (black), 0.3 m (blue), 0.6 m (red), and 0.9 m (magenta).

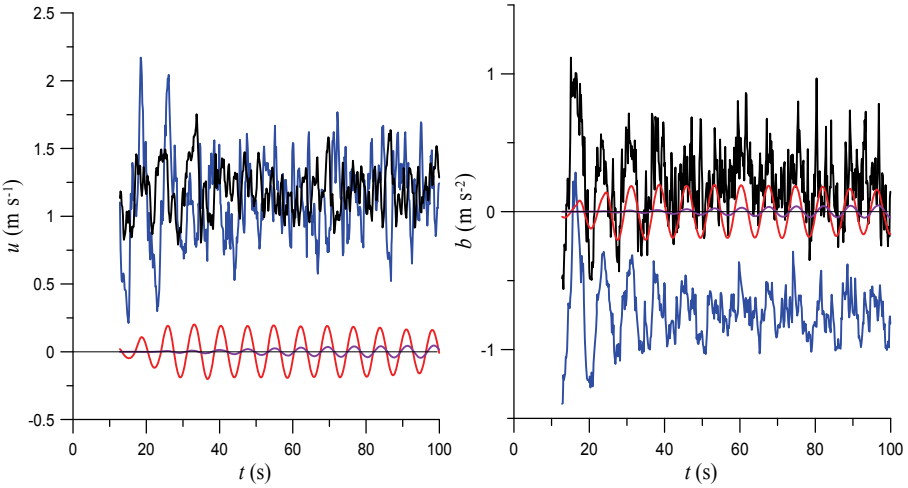

Fig. 5. Temporal evolution of the (x-y) plane-averaged velocity (left plot) and buoyancy (right plot) fields in the anabatic flow with $B_s = 0.5$ m^{2}s^{-3}, $\nu = 10^{-4}$ m^{2}s^{-1}, and $N = 1$ s^{-1} (Fp$_B = 5000$) along a 60°-slope at four different distances from the slope: 0.12 m (black), 0.24 m (blue), 0.75 m (red), and 1.0 m (magenta).

Also, as in the katabatic flow case, the depth of the thermal boundary layer is considerably smaller than that of the dynamic boundary layer. The latter feature is revealed by comparison of relative buoyancy and velocity changes over the interval of heights between $z = 0.12$ m and $z = 0.24$ m. Note that the

average velocity remains positive and approximately constant between these two layers, whilst the average buoyancy changes from a slightly positive value to a relatively large negative value which corresponds to the negatively buoyant flow above the thermal boundary layer. A comparison of the velocity time series in Fig. 5 and Fig 4 also reveals that momentum in the turbulent region of the anabatic flow is distributed vertically more uniformly than in the core of the katabatic flow. Inspection of the evolution of velocity and buoyancy oscillations at large distances from the slope ($z = 0.75$ m and $z = 1.0$ m) indicates that there is a delay of the wavy motion development in the remote flow regions. This delay is increasing with distance from the wall: flow oscillations at $z = 1.0$ m develop noticeably later than at $z = 0.75$ m.

4.3 Mean-flow and turbulence structure

Figure 6 shows the mean flow profiles of momentum and buoyancy in katabatic and anabatic flows with the same absolute value of the flow forcing parameter Fp_B along slopes of three different angles. The mean profiles were obtained by averaging the simulated flow fields spatially over x-y planes and temporally over at least 7 oscillation periods beyond the transition stage. The plots in Fig. 6 illustrate the slope-angle dependence of the mean structure of the turbulent flows. The structural features of these flows can be compared to those of the Prandtl slope flow (Section 3.2). The velocity and buoyancy profiles in Fig. 6 show considerable sensitivity to the slope angle for both katabatic and anabatic flow cases. The shape of the katabatic-flow velocity profile for both slope angles less than $\alpha = 90°$ is very different from the shape of the velocity profile in the anabatic flow. Differences in shape between the buoyancy profiles for both flow cases are less pronounced which is partially due to the fact that in both flow cases the buoyancy sharply drops (increases) in the very close vicinity of the wall. Buoyancy and velocity profiles in the simulated katabatic flows very closely resemble their counterparts observed in the field study of katabatic flow by Monti *et al*. (2002; Fig. 9a).

In the katabatic flow, stable environmental stratification in combination with negative surface buoyancy forcing lead to an effective suppression of vertical turbulent exchange in the flow region in the immediate vicinity of the slope. Associated with this shallow layer of strong negative buoyancy is a narrow mean-velocity jet with peak velocity found at very low levels. The magnitude of this jet increases with decreasing slope angle, thus revealing a qualitative similarity to the same feature of the velocity profile in the Prandtl model (right plot of Fig. 2).

However, due to the stronger impedance of the slope-normal motions by the negative buoyancy in the case of more shallow slope (see eq. 3), the jet maximum in the numerically simulated katabatic flow does not shift away

from the slope with decreasing α as noticeably as in the Prandtl model (right plot of Fig. 2). Another structural feature of the turbulent katabatic flow that is similar to the Prandtl-model flow is the increase of the surface buoyancy magnitude with decreasing slope angle. A sharpness of the near-surface buoyancy increase in the turbulent katabatic flow is apparently enhanced by the suppression of vertical exchange of heat (buoyancy) by hydrostatic stability effects. Because of the aforementioned features of the momentum and buoyancy transport in the near-surface region of the katabatic flow, the resulting jet is much more asymmetric in the simulated turbulent katabatic flow than in the Prandtl flow.

Structurally, the simulated anabatic flows differ from their katabatic counterparts primarily with respect to the shape, magnitude and vertical extension of the jet. In the near-surface region of the anabatic flow, the positive surface buoyancy flux acts as a turbulence production mechanism. In combination with shear generation of turbulence, it opposes the turbulence destruction effect of the stable stratification. The interaction between these three turbulence generation/destruction mechanisms results in a vertical mixing of momentum in the anabatic jet that becomes more efficient with a decreasing slope angle. This happens because the surface buoyancy production apparently offsets the suppressing effect of stratification on the turbulent exchange in the slope-normal direction more effectively as slope angle decreases and leads to the enhancement of vertical mixing. The effect of this enhanced mixing is also seen in the reduced values of the surface buoyancy profiles for the anabatic flow case and a near independence of the surface buoyancy on the angle. These turbulence effects make turbulent anabatic flow differ more, in a mean qualitative sense, from its Prandtl model analog than the counterpart katabatic flow.

Notably, despite all these structural differences, the overall vertical extension of the mean flow disturbance in terms of velocity appears to be practically the same for katabatic and anabatic flows along slopes of the same angle. Furthermore, direct evaluation of the integrals of mean velocity profiles shown in Fig. 6 confirms validity of the earlier obtained integral dynamic similarity constraint (18) for the simulated slope flow cases. In particular, the velocity profiles in Fig. 6 that correspond to the same α should integrate to the same value as they indeed do. In addition, the velocity integrals for the same values of B_s and N but for different slope angles relate as ratios of the sines of slope angles.

As revealed by the buoyancy variance profiles in Fig. 7, the buoyancy fluctuations in both katabatic and anabatic flow cases attain their maximum magnitude extremely close to the wall, within the region where maximum gradients are observed in the mean buoyancy profiles (Fig. 6). The drop of $\overline{b'b'}$

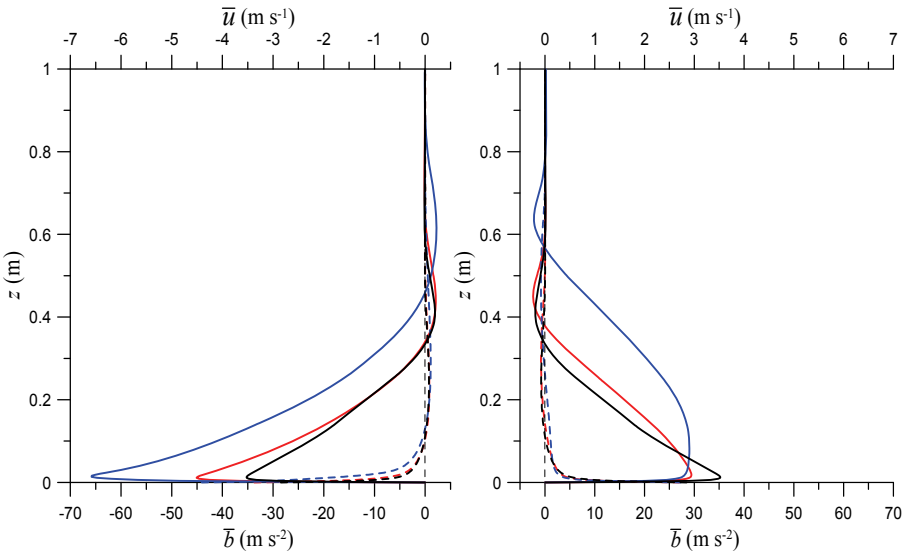

Fig. 6. Mean along-slope velocity (u, solid lines) and buoyancy (b, dashed lines) profiles in the katabatic (left) and anabatic (right) flows with $|B_s| = 0.5$ m^{2}s^{-3}, $\nu = 10^{-4}$ m^{2}s^{-1}, and $N = 1$ s^{-1} ($|\mathrm{Fp}_B| = 5000$) for three different slope angles: 30° (blue lines), 60° (red lines), and 90° (black lines).

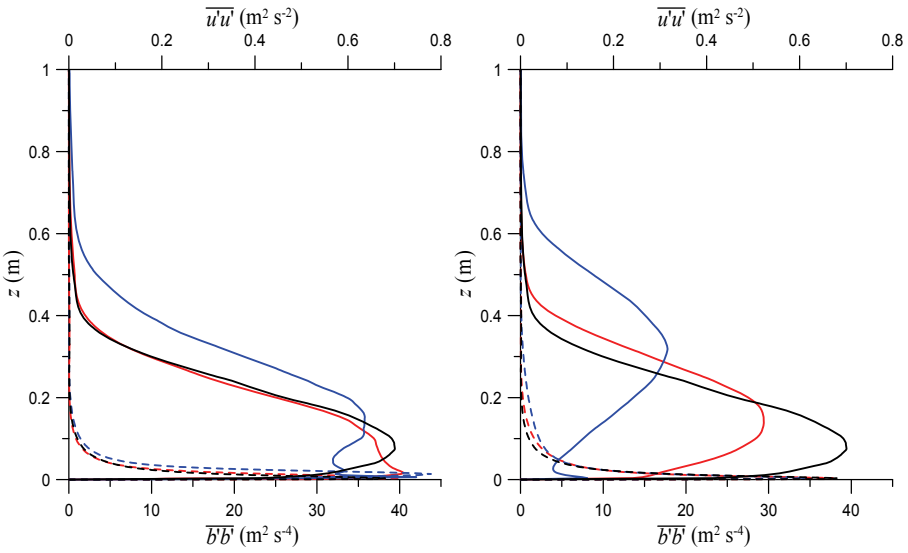

Fig. 7. Slope angle dependence of the along-slope velocity (solid lines) and buoyancy (dashed lines) variances in the katabatic (left) and anabatic (right) flows presented in Fig. 6.

beyond the maximum is also rather sharp which means that significant fluctuations of the buoyancy are restricted to a comparatively thin near-wall layer. The variance magnitudes are larger in the katabatic flows compared to the variances in anabatic flows with the same $|\mathrm{Fp}_B|$ value. The buoyancy variance decay with distance from the wall displays a clear slope-angle dependence. This decay is weaker in the anabatic flows, which apparently is a result of the increasing contribution to the variance from buoyancy-related turbulent mixing with smaller slope angles. In the katabatic flow, the increase of variance caused by larger near-surface mean buoyancy gradient at smaller slope angles is partially offset by stronger damping of turbulence by stratification as the slope angle decreases, so the resulting decay of $\overline{b'b'}$ with z is only slightly weaker in the case of a relatively shallow slope ($\alpha = 30°$) than in the case of a steeper slope ($\alpha = 60°$) and the vertical wall case ($\alpha = 90°$).

Along-slope velocity fluctuations of notable magnitudes are distributed over layers that are typically a few times thicker than the layers which contain most of the buoyancy variance in both the katabatic and anabatic flow cases (see profiles of velocity variance $\overline{u'u'}$ in Fig. 7). In both flow cases, a tendency to develop narrow secondary maxima of $\overline{u'u'}$ in the close vicinity of the slope is observed. These secondary maxima, which are not found in the flow along a vertical wall ($\alpha = 90°$), become more pronounced with decreasing slope angle and are more prominent in katabatic flow (in the anabatic flow with a 60° slope, a near-surface bend in the $\overline{u'u'}$ profile rather than a maximum is observed). After $\overline{u'u'}$ reaches its global maximum for any individual slope case, it decays away from the slope in a more gradual manner than the $\overline{b'b'}$ variance.

As may be concluded from the profiles of slope-normal fluxes of momentum, $\overline{u'w'}$, and buoyancy, $\overline{b'w'}$, in Fig. 8, zero crossings in the mean profiles of b and u are closely co-located with the minima and maxima of the fluxes $\overline{u'w'}$ and $\overline{b'w'}$. This co-location is in agreement with inviscid forms of (15) and (16) for any z except for locations very close to the wall, where molecular effects are important. Typically, molecular fluxes in the simulated flows become negligible at distances from the surface that are significantly smaller than the elevations of the mean velocity maxima (jet elevations). Narrow near-surface bands of positive (negative) momentum flux in katabatic (anabatic) flow correspond to the flow regions where negative (positive) momentum is transported to the wall (that is, in the $-z$ direction). As may be additionally deduced from relating profiles of velocity and buoyancy in Fig. 6 to profiles of momentum and turbulent fluxes in Fig. 8, the ordinates

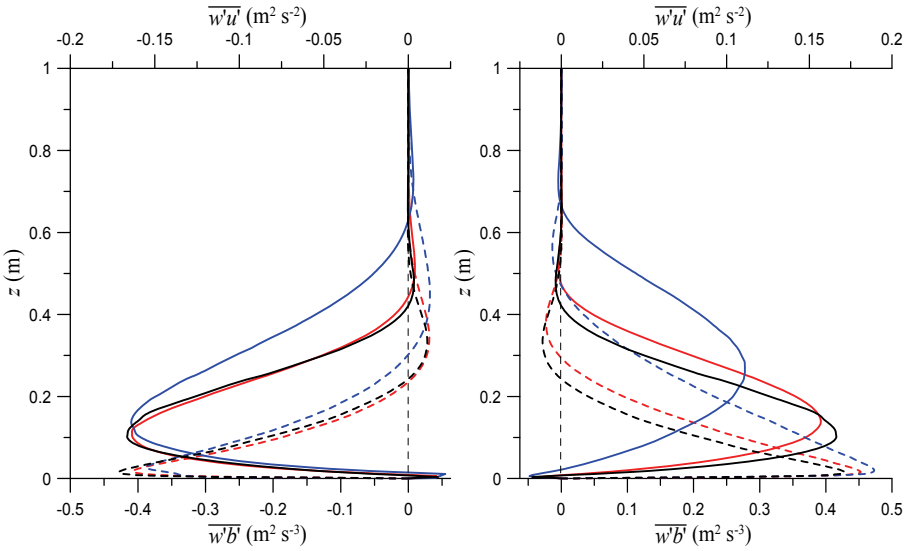

Fig. 8. Slope angle dependence of the kinematic turbulent momentum (solid lines) and buoyancy (dashed lines) fluxes in the katabatic (left) and anabatic (right) flows presented in Fig. 6.

of zero fluxes are closely co-located with the ordinates of zero gradients of the corresponding mean profiles. These flow features imply that turbulent fluxes are in apparent anti-correlation with the corresponding mean gradients for both simulated flow types. Therefore, turbulent transport in these katabatic and anabatic flows allows a description in terms of uniquely defined positive proportionality coefficients (eddy viscosities and diffusivities). We conducted a preliminary evaluation of the slope-normal of the turbulent Prandtl number (which is the ratio of the eddy viscosity to the eddy diffusivity) for one of simulated katabatic flow cases and found that, except for the region of very strong static stability close to the surface, the Prandtl number values do not significantly depart from unity over the main portion of the flow and are within the ranges observed by Monti *et al.* (2002).

Interestingly, the magnitude of $\overline{u'w'}$ for the katabatic flow case shows very weak dependence on the slope angle − in sharp contrast to the momentum flux behavior in the anabatic flow case where it is characterized by relatively strong decay of the flux magnitude and upward shift of the flux maximum with decreasing slope angle. On the other hand, the shapes of the $\overline{b'w'}$ profiles in katabatic and anabatic flows show some degree of similarity with respect to the dependence on the slope angle. In both cases, the buoyancy flux magnitude increases as the slope angle decreases.

Flux profiles shown in Fig. 8 indicate that there is no region in the flow domain with constancy (even approximate) of any flux with distance from the wall. Arguably, this may be a specific feature of the slope flows in the presence of ambient stratification. In more conventional boundary-layer type flows, the existence of height intervals with slowly changing (in the first approximation, constant) momentum and buoyancy fluxes is used as a foundation for similarity analyses and scalings (Tennekes and Lumley 1972). Such a constant-flux formalism does not apply, at least in a straightforward manner, to the slope flows considered in our study.

On a related note, we have not found any evidence of scale separation in the simulated flows that would allow the flow to be subdivided into regions where any of the governing parameters (B_s, ν, N, or α) could be dropped from consideration. Even at relatively large distances from the slope, the molecular viscosity/diffusivity in combination with the surface buoyancy flux influence the local flow structure through the near-wall peak velocity value that is directly determined by their combined effect. On the other hand, the ambient stratification (in terms of N) is started to be felt in the immediate vicinity of the wall, so it is impossible to isolate a flow region where the dependence on N may be neglected. These conclusions are consistent with the flow parameter considerations presented in Section 4.1.

The development of velocity fluctuations normal to the wall (w') is apparently hampered by the presence of the wall. This explains the relatively slow growth with z and smaller values of $\overline{w'w'}$ in Fig. 9 as compared to $\overline{u'u'}$ in Fig. 7 and $\overline{v'v'}$ in Fig. 9. Curiously, profiles of the latter variance consistently display secondary maxima very close to the wall. This feature is reminiscent of the previously discussed maxima in the $\overline{u'u'}$ distributions (Fig. 7). On the whole, the $\overline{v'v'}$ profiles are generally rather similar to the $\overline{u'u'}$ profiles, especially in the case of anabatic flow. However, unlike the $\overline{u'u'}$ variance, secondary maxima of $\overline{v'v'}$ are found also in the flows along a vertical wall. It is our guess that these noted features of the velocity component variances may be associated with the influence of internal gravity waves (discussed in Section 4.2) whose effect on the spatial distribution of velocity fluctuations in the near-surface flow region apparently depends on the slope angle. To quantitatively explain the secondary maxima in $\overline{u'u'}$ and $\overline{v'v'}$, the estimates of second-order turbulence moment budgets would be needed, but those are not available at this point.

We now analyze the influence of the magnitude of the surface forcing (the surface buoyancy flux B_s) on the mean velocity and buoyancy profiles (Fig. 10) and turbulence structure parameters (Figs. 11 and 12).

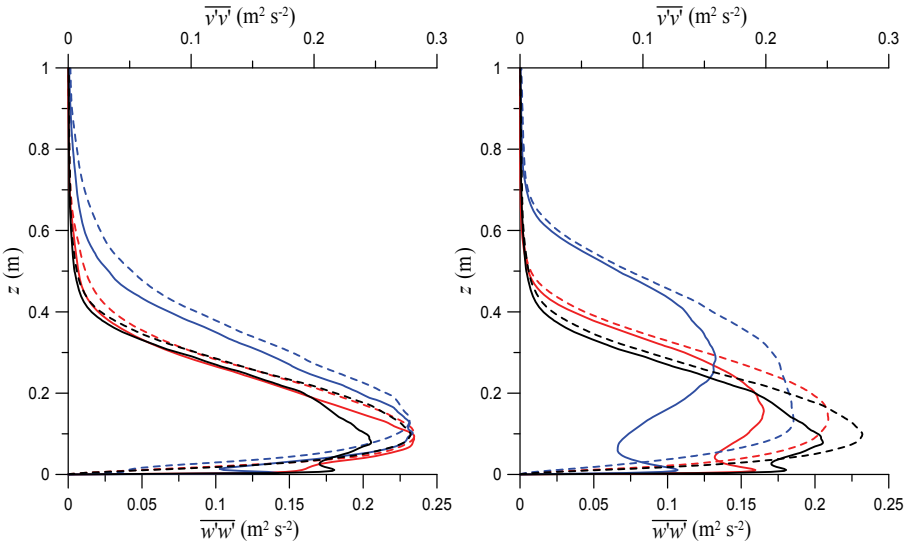

Fig. 9. Slope angle dependence of the variance of the v (solid lines) and w (dashed lines) velocity components in the katabatic (left) and anabatic (right) flows presented in Fig. 6.

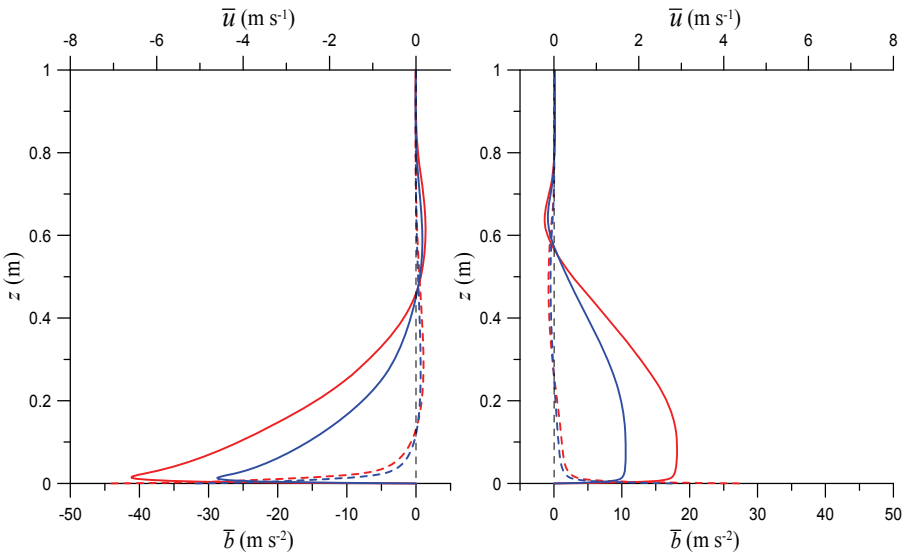

Fig. 10. Mean u (solid lines) and b (dashed lines) profiles in the katabatic (left) and anabatic (right) flows along 30° slope with $\nu = 10^{-4}$ m^{2}s^{-1}, $N = 1$ s^{-1}, and two different surface forcing magnitudes: $|B_s| = 0.3$ m^{2}s^{-3} ($|\mathrm{Fp}_B| = 3000$, blue lines) and $|B_s| = 0.5$ m^{2}s^{-3} ($|\mathrm{Fp}_B| = 5000$, red lines).

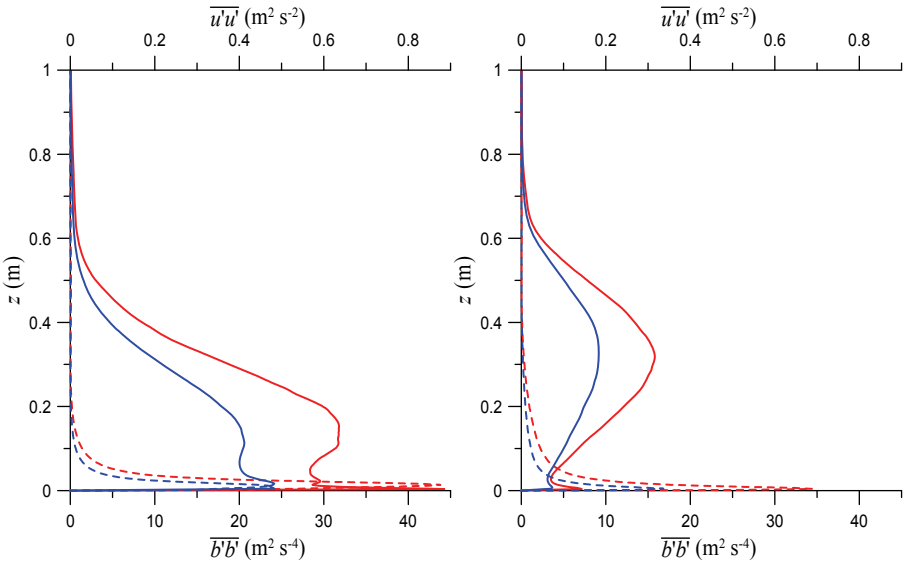

Fig. 11. Surface forcing dependence of the along-slope velocity (solid lines) and buoyancy (dashed lines) variances in the katabatic (left) and anabatic (right) flows presented in Fig. 10.

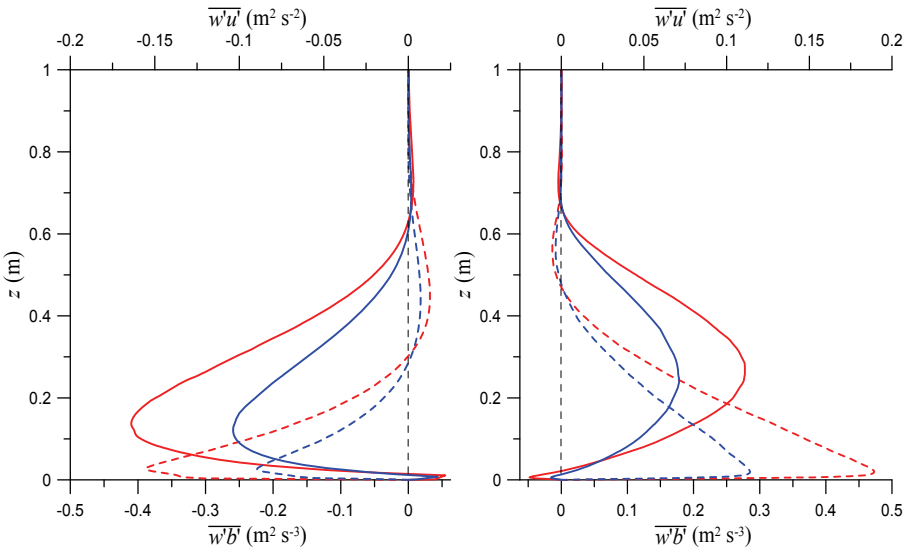

Fig. 12. Surface forcing dependence of the kinematic turbulent fluxes of momentum (solid lines) and buoyancy (dashed lines) in the katabatic (left) and anabatic (right) flows presented in Fig. 10.

The differences between the buoyancy profiles corresponding to different B_s are largest in the close vicinity of the slope. With $|B_s| = 0.5$ m^{2}s^{-3}, the magnitude of the surface buoyancy value, $|b_s|$, in the katabatic flow case is 1.38 times larger than with $|B_s| = 0.3$ m^{2}s^{-3}. The corresponding increase in the anabatic flow case is 1.56. This difference points to distinctively different and non-linear scaling relationships between B_s and b_s in katabatic and anabatic flows. The difference in depth between the thermal and dynamic boundary layers in the katabatic (anabatic) flow, already noted above, is clearly seen from comparing the rate of buoyancy growth (decay) with distance from the wall to that of velocity after it reached its minimum in the vicinity of the wall.

Although there are obvious differences in detail between the mean velocity and buoyancy profiles in the turbulent katabatic flow (left plot of Fig. 10) and the corresponding laminar (Prandtl-model) flow profiles in Fig. 2, the overall mean flow structure is qualitatively the same: cold (relative to environment) fluid descends along the slope, whilst warm fluid rises upslope at some distance from the slope. The anabatic flow (right plot of Fig. 10) displays a more anti-symmetric structure, with the reverse flow (which is directed down-slope in this case) being shallower and the upslope current (shaped as a broad jet) being deeper than in the katabatic flow. However, according to the previously established integral dynamic similarity constraint (eq. 20), the integrals of the velocity profiles in Fig. 10 scale with $|B_s|$ for both katabatic and anabatic flow cases shown.

A striking feature of the mean flow profiles shown in Fig. 10 is a very weak dependence (in practical terms − independence) of their vertical scales on the magnitude of surface forcing B_s. Indeed, vertical changes of velocity and buoyancy profiles in flows with different B_s are closely coordinated for each flow type. This implies that the vertical flow length scale for either flow type with fixed values of ν, N, and α is practically independent of $|B_s|$. An analogous behavior is displayed by the profiles of turbulence statistics shown in Figs. 11 and 12. The positions of minima/maxima and zero-crossover heights of profiles corresponding to different B_s values practically coincide for a given slope flow type, showing a minimal dependence on the B_s magnitude. To further investigate this weak depth-scale dependence of slope flows on the surface energy production rate, additional numerical experiments with B_s values varying in broader ranges will be needed.

5. SUMMARY AND CONCLUSIONS

In this study, buoyantly driven slope flows along doubly-infinite cooled/heated inclined surfaces immersed in a stably-stratified fluid have been reexamined within the conceptual framework of the Prandtl (1942)

slope-flow model, and numerically investigated by means of DNS. The numerically simulated flows, driven by a spatially-uniform surface buoyancy flux B_s (energy production rate), were moderately turbulent, with characteristic integral Reynolds numbers in the range from 3000 to 10,000. These DNS complement previous numerical large eddy simulations of katabatic/anabatic flows reported in the literature.

Solutions of the Prandtl model with prescribed surface forcing in the form of constant buoyancy flux were obtained. (The original Prandtl solutions correspond to slope-flow cases with prescribed constant surface buoyancy.) It was found that the surface buoyancy value as well as the elevation and intensity of the velocity maximum increase with decreasing slope angle as $\sin^{-1/2}\alpha$. A corresponding scaling has been proposed for the Prandtl model flow that incorporates dependence of the buoyancy and velocity profiles on the slope angle.

Numerical experiments show that following the transition from a laminar to a turbulent regime, the simulated katabatic and anabatic flows enter quasi-stationary oscillatory phases. The frequency of the ensuing perpetual oscillations (associated with internal gravity waves) is given by the product of the environmental Brunt–Väisälä frequency and the sine of the slope angle, $N\sin\alpha$, which is in a direct agreement with known hydraulic model predictions and field observations of slope flows. In both simulated flow types (katabatic flow with $B_s < 0$ and anabatic flow with $B_s > 0$), the turbulent fluctuations gradually fade with distance from the wall, while periodic oscillations persist within outer laminar flow regions before fading out.

Notably, these oscillatory flow regimes are found under the conditions of temporally constant surface buoyancy forcing. They are characterized by strong interactions between turbulent and wavy motions that apparently result in peculiar structural flow features. For instance, the slope-parallel velocity component variances consistently display secondary maxima very close to the wall, at distances comparable to those of the mean velocity maxima/minima. An explanation of this and other turbulence structure features would require estimates of the second-order turbulence moment budgets in the simulated flow and analyses of the turbulence spectra.

The mean (averaged over time and wall-parallel planes) structure of the simulated flows is dependent on a dimensionless combination of governing parameters given by $\mathrm{Fp}_B \equiv B_s \nu^{-1} N^{-2}$, which may be interpreted as a flow forcing parameter. The sign of Fp_B is determined by the slope flow type. It is negative for katabatic flow ($B_s < 0$) and positive for anabatic flow ($B_s > 0$). The magnitude of Fp_B represents the ratio between the energy production at the surface and the work against buoyancy and viscous forces. The integral Reynolds number Re_I of the flow is related to the magnitude of Fp_B as Re_I

$\mathrm{Re}_I = |\mathrm{Fp}_B|/\sin\alpha$, so for a given slope angle, one may expect turbulence in the slope flow to be more developed with larger $|\mathrm{Fp}_B|$ values. Scaling analysis indicates that for a given slope angle α, any expressions for length, velocity, and buoyancy scales which result in the same $\mathrm{Fp}_B \equiv B_s \nu^{-1} N^{-2}$, should yield normalized profiles of velocity, buoyancy, and corresponding turbulent fluxes that are universal functions of the normalized distance from the slope.

The integral dynamic similarity constraint,

$$\int_0^\infty \overline{u}\,\mathrm{d}z = B_s/(N^2\sin\alpha) = \mathrm{Fp}_B\,\nu/\sin\alpha\,,$$

was derived from the averaged thermal energy (buoyancy balance) equation and quantitatively verified against the DNS data. Notably, this constraint applies to both turbulent and laminar slope flows as well as to both katabatic and anabatic flows.

With respect to their basic structural features, the mean katabatic and anabatic flows appear similar to the corresponding laminar (Prandtl) counterparts. In the turbulent katabatic flow, cool (relative to environment) fluid descends along the sloping surface, whilst warm fluid moves upslope at some distance from the surface. In the turbulent anabatic flow, warm (relative to environment) fluid rises along the sloping surface, whilst cool fluid moves down-slope at larger distances from the slope. Structurally, the mean katabatic turbulent flow is more similar to the Prandtl slope flow than the mean anabatic flow with the same $|\mathrm{Fp}_B|$ and α.

Close down-gradient relations between the turbulent fluxes and corresponding gradients of mean fields have been observed in the simulated turbulent slope flows. No flow region has been identified with constancy (even approximate) of any of the fluxes with distance from the wall. No evidence has been found of scale separation in the simulated flow cases that would allow the flow to be subdivided into regions where any of governing parameters (B_s, ν, N, or α) could be dropped from consideration.

The flow scale in the slope-normal direction shows very weak (almost non-existing in terms of the mean velocity and buoyancy profiles) dependence on the magnitude of surface forcing, so that changes of $\overline{u}$ and $\overline{b}$ with z for the same flow type are closely coordinated for different B_s. An analogous behavior is found in the corresponding profiles of the turbulence statistics.

Acknowledgement. This research was supported, in part, by the National Science Foundation, USA, through the grant ATM-0622745.

References

Atkinson, B.W. (1981), *Meso-Scale Atmospheric Circulations*, Academic Press, London, 495 pp.

Ball, F.K. (1956), The theory of strong katabatic winds, *Aust. J. Phys.* **9**, 373-386.

Batchelor, G.K. (1967), *An Introduction to Fluid Dynamics*, Cambridge University Press, Cambridge, 615 pp.

Brazel, A.J., H.J.S. Fernando, J.C.R. Hunt, N. Selover, B.C. Hedquist, and E. Pardyjak (2005), Evening transition observations in Phoenix, Arizona, *J. Appl. Meteorol.* **44**, 99-112, DOI: 10.1175/JAM-2180.1

Bromwich, D.H., J.J. Cassano, T. Klein, G. Heinemann, K.M. Hines, K. Steffen, and J.E. Box (2001), Mesoscale modeling of katabatic winds over Greenland with the Polar MM5, *Monthly Weath. Rev.* **129**, 2290-2309, DOI: 10.1175/1520-0493(2001)129<2290:MMOKWO>2.0.CO;2.

Defant, F. (1949), Zur Theorie der Hangwinde, nebst Bemerkungen zur Theorie der Berg- und Talwinde, *Arch. Met. Geophys. Bioklim. A* **1**, 421-450 (in German).

Ekman, V.W. (1905), On the influence of the earth's rotation on ocean currents, *Ark. Mat. Astron. Fysik* **2**, 1-53.

Elder, J.W. (1965), Laminar free convection in a vertical slot, *J. Fluid Mech.* **23**, 77-98, DOI: 10.1017/S0022112065001246.

Fedorovich, E., and A. Shapiro (2009), Turbulent natural convection along a vertical plate immersed in a stably stratified fluid, *J. Fluid Mech*. (in press).

Fernando, H.J.S., S.M. Lee, J. Anderson, M. Princevac, E. Pardyjak, and S. Grossman-Clarke (2001), Urban fluid mechanics: air circulation and contaminant dispersion in cities, *Environ. Fluid Mech.* **1**, 107-164, DOI: 10.1023/A:1011504001479.

Gallée, H., and G. Schayes (1994), Development of a 3-dimensional meso-γ primitive equation model: Katabatic winds simulation in the area of Terra Nova Bay, Antarctica, *Monthly Weath. Rev.* **122**, 671-685, DOI: 10.1175/1520-0493(1994)122<0671:DOATDM>2.0.CO;2.

Gill, A.E. (1966), The boundary-layer regime for convection in a rectangular cavity, *J. Fluid Mech.* **26**, 515-536, DOI: 10.1017/S0022112066001368.

Heinemann, G., and T. Klein (2002), Modelling and observations of the katabatic flow dynamics over Greenland, *Tellus A* **54**, 542-554, DOI: 10.1034/j.1600-0870.2002.201401.x.

Hunt, J.C.R., H.J.S. Fernando, and M. Princevac (2003), Unsteady thermally driven flows on gentle slopes, *J. Atmos. Sci.* **60**, 2169-2182, DOI: 10.1175/1520-0469(2003)060<2169:UTDFOG>2.0.CO;2.

Klein, T., G. Heinemann, D.H. Bromwich, J.J. Cassano, and K.M. Hines (2001), Mesoscale modeling of katabatic winds over Greenland and comparisons with AWS and aircraft data, *Meteor. Atmos. Phys.* **78**, 115-132, DOI: 10.1007/s007030170010.

Langhaar, H.L. (1951), *Dimensional Analysis and Theory of Models*, Robert E. Krieger Publishing Company, Malabar, FL, 166 pp.

Lee, S.M., H.J.S. Fernando, M. Princevac, D. Zajic, M. Sinesi, J.L. McCulley, and J. Anderson (2003), Transport and diffusion of ozone in the nocturnal and morning planetary boundary layer of the Phoenix valley, *Environ. Fluid Mech*. **3**, 331-362, DOI: 10.1023/A:1023680216173.

Lu, R., and R.P. Turco (1994), Air pollutant transport in a coastal environment. Part I: Two-dimensional simulations of sea-breeze and mountain effects, *J. Atmos. Sci.* **51**, 2285-2308, DOI: 10.1175/1520-0469(1994)051<2285:APTIAC> 2.0.CO;2.

Monti, P., H.J.S. Fernando, M. Princevac, W.C. Chan, T.A. Kowalewski, and E.R. Pardyjak (2002), Observations of flow and turbulence in the nocturnal boundary layer over a slope, *J. Atmos. Sci.* **59,** 2513-2534, DOI: 10.1175/ 1520-0469(2002)059<2513:OOFATI>2.0.CO;2.

Nappo, C.J., and K.S. Rao (1987), A model study of pure katabatic flows, *Tellus A* **39**, 61-71.

Oerlemans, J. (1998), The atmospheric boundary layer over melting glaciers. **In:** A.A.M. Holtslag and P.G. Duynkerke (eds.), *Clear and Cloudy Boundary Layers*, Royal Netherlands Academy of Arts and Sciences, Amsterdam, 129-153.

Papadopoulos, K.H., C.G. Helmis, A.T. Soilemes, J. Kalogiros, P.G. Papageorgas, and D.N. Asimakopoulos (1997), The structure of katabatic flows down a simple slope, *Quart. J. Roy. Met. Soc.* **123**, 1581-1601, DOI: 10.1002/qj. 49712354207.

Parish, T.R. (1984), A numerical study of strong katabatic winds over Antarctica, *Monthly Weath. Rev.* **112**, 545-554, DOI: 10.1175/1520-0493(1984)112 <0545:ANSOSK>2.0.CO;2.

Parish, T.R., and K.T. Waight (1987), The forcing of antarctic katabatic winds, *Monthly Weath. Rev.* **115**, 2214-2226, 10.1175/1520-0493(1987)115<2214: TFOAKW>2.0.CO;2

Peacock, T., R. Stocker, and M. Aristoff (2004), An experimental investigation of the angular dependence of diffusion-driven flow, *Phys. Fluids* **16**, 3503-3505, DOI: 10.1063/1.1763091.

Phillips, O.M. (1970), On flows induced by diffusion in a stably stratified fluid, *Deep-Sea Res.*, **17**, 435-443.

Pope, S.B. (2000), *Turbulent Flows*, Cambridge University Press, Cambridge, 771 pp.

Prandtl, L. (1942), *Führer durch die Strömungslehre*, Vieweg und Sohn, Braunschweig, 382 pp. (in German).

Rampanelli, G., D. Zardi, and R. Rotunno (2004), Mechanisms of up-valley winds, *J. Atmos. Sci.* **61**, 3097-3111, DOI: 10.1175/JAS-3354.1.

Princevac, M., J.C.R. Hunt, and H.J.S. Fernando (2008), Quasi-steady katabatic winds on slopes in wide valleys: Hydraulic theory and observations, *J. Atmos. Sci.* **65**, 627-643, DOI: 10.1175/2007JAS2110.1.

Renfrew, I.A. (2004), The dynamics of idealized katabatic flow over a moderate slope and ice shelf, *Quart. J. Roy. Met. Soc.* **130**, 1023-1045, DOI: 10.1256/qj.03.24.

Schumann, U. (1990), Large-eddy simulation of the up-slope boundary layer, *Quart. J. Roy. Met. Soc.* **116**, 637-670, DOI: 10.1256/smsqj.49306.

Shapiro, A., and E. Fedorovich (2004a), Unsteady convectively driven flow along a vertical plate immersed in a stably stratified fluid, *J. Fluid Mech*. **498**, 333-352, DOI: 10.1017/S0022112003006803.

Shapiro, A., and E. Fedorovich (2004b), Prandtl-number dependence of unsteady natural convection along a vertical plate in a stably stratified fluid, *Int. J. Heat Mass Transfer* **47**, 4911-4927, DOI: 10.1016/j.ijheatmasstransfer.2004.04.035.

Shapiro, A., and E. Fedorovich (2005), Analytical and numerical study of natural convection in a stably stratified fluid along vertical plates and cylinders with temporally-periodic surface temperature variations. **In:** R. Bennacer, A.A. Mohamad, M. El Ganaoui, and J. Sicard (eds.), *Progress in Computational Heat and Mass Transfers*, vol. 1, Lavoisier, Paris, 77-82.

Shapiro, A., and E. Fedorovich (2006), Natural convection in a stably stratified fluid along vertical plates and cylinders with temporally-periodic surface temperature variations, *J. Fluid Mech*. **546**, 295-311, DOI: 10.1017/S0022112005007159.

Shapiro, A., and E. Fedorovich (2007), Katabatic flow along a differentially cooled sloping surface, *J. Fluid Mech*. **571**, 149-175, DOI: 10.1017/S0022112006003302.

Shapiro, A., and E. Fedorovich (2008), Coriolis effects in homogeneous and inhomogeneous katabatic flows, *Quart. J. Roy. Met. Soc.* **134**, 353-370, DOI: 10.1002/qj.217.

Shchepetkin, A.F., and J.C. McWilliams (1998), Quasi-monotone advection schemes based on explicit locally adaptive dissipation, *Monthly Weath. Rev.* **126**, 1541-1580, DOI: 10.1175/1520-0493(1998)126<1541:QMASBO>2.0.CO;2.

Skyllingstad, E.D. (2003), Large-eddy simulation of katabatic flows, *Bound.-Layer Meteor.* **106**, 217-243, DOI: 10.1023/A:1021142828676.

Tennekes, H., and J.L. Lumley (1972), *A First Course in Turbulence*, The MIT Press, Cambridge, MA, 300 pp.

Tyson, P.D. (1968), Velocity fluctuations in the mountain wind, *J. Atmos. Sci.* **25**, 381-384, DOI: 10.1175/1520-0469(1968)025<0381:VFITMW>2.0.CO;2.

Veronis, G. (1970), The analogy between rotating and stratified fluids, *Ann. Rev. Fluid Mech.* **2**, 37-66, DOI: 10.1146/annurev.fl.02.010170.000345.

Wunsch, C. (1970), On oceanic boundary mixing, *Deep-Sea Res.* **17**, 293-301.

Received 25 March 2009
Accepted 16 July 2009